Climate Dynamics (2026) 64:164
https://doi.org/10.1007/s00382-026-08134-y

DAMV: a symbiotic fingerprint of AMV unveiled from the deep Atlantic

Jiajun Yang[1] · Jianping Li[1,2] · Qirong An[1,2] · Leon Hermanson[3]

Received: 27 September 2025 / Accepted: 4 March 2026

Abstract
The Atlantic meridional overturning circulation (AMOC), a critical component of the global thermohaline circulation, governs meridional heat transport, and connects the sea surface and deep Atlantic. Yet, its dynamical role in the Atlantic multidecadal variability (AMV) and Deep atlantic multidecadal variability (DAMV) remains elusive. We identify a statistically robust coupling between AMV and DAMV, and such coupling supports the interpretation of DAMV as a deep-ocean symbiotic fingerprint of AMV. We further reveal an asymmetric temporal loop: DAMV leads AMV by approximately 1 decade but lags it by 2 to 3 decades, which could be served as deep-ocean connection between AMV phase transition in spatial pattern. This delayed interaction mirrors AMOC-driven ocean heat transport (OHT), particularly the temperature-induced OHT. Our findings demonstrate that AMV and DAMV form a delayed coupled vertical system for the first time, underscoring the importance of deep-ocean dynamics for improving coupled climate prediction on decadal timescales.

Keywords Atlantic multidecadal variability · Deep Atlantic multidecadal variability · Atlantic meridional overturning circulation

1 Introduction

The ocean has slowed Earth's surface warming over the past century through deep-ocean heat storage (Chen and Tung 2014; Cheng et al. 2022; Li et al. 2023; Oh et al. 2024). The Atlantic Ocean stands out due to the presence of the Atlantic meridional overturning circulation (AMOC), a large-scale circulation system characterized by a northward surface transporting warm salty water into the high-latitude North Atlantic, where it then sinks and returns southward as a cold fresh water in the deep Atlantic (Schmitz 1995; Marshall and Schott 1999; Buckley and Marshall 2016; Terhaar et al. 2025). Due to the pronounced role in heat and freshwater transports, the AMOC drives global climate phenomena with major societal and economic impacts, including regional climate across North America, Europe, and Asia; and hemispheric-scale surface temperature warming (Zhang et al. 2019). The AMOC serves as a crucial connect linking the two hemispheres by meridional transporting 17 Sverdrups approximately accompanied by variations within a range of ± 2 based on the observation and models (Jackson et al. 2022). In this context, the AMOC is a dominant driver of interhemispheric ocean heat transport (OHT), which has a substantial influence on sea surface temperature (SST) and deep-sea potential temperature (DSPT) variability in the Atlantic Ocean, particularly at low-frequency timescales (Trenberth and Caron 2001; Collins et al. 2006).

Pertaining to the Atlantic SST field, basin scale low-frequency variability has traditionally been referred to as Atlantic multidecadal oscillation, which is commonly defined by the area weighted average SST over the North Atlantic, basically 0° to 70N°. As time goes by, given its broader significant low-frequency spectral characteristics, the term Atlantic multidecadal variability (AMV) is now more appropriately used (Sutton et al. 2018; Zhang et al. 2019). The AMV is characterized by a dipole pattern, with warming (cooling) over the North Atlantic and relatively weaker cooling (warming) over the South Atlantic during the positive (negative) phase (Latif et al. 2006; Roberts et

✉ Jianping Li
ljp@ouc.edu.cn

[1] Frontiers Science Center for Deep Ocean Multi-Spheres and Earth System (DOMES)/ Key Laboratory of Physical Oceanography/ Academy of Future Ocean/ College of Oceanic and Atmospheric Sciences, Ocean University of China, Qingdao 266100, China

[2] Laoshan Laboratory, Qingdao 266237, China

[3] Met Office Hadley Centre, Exeter, UK

Published online: 27 March 2026

al. 2013; Zhang et al. 2013). Despite the robustness of the AMV signal derived from observation and model simulations, the underlying physical mechanisms of the AMV and the relative importance of each remain under active debate, encompassing the AMOC-related oceanic processes (Yan et al. 2017; Zhang 2017; Yan et al. 2018; Sun et al. 2019), ocean–atmosphere coupling dynamics (Clement et al. 2015; Wills et al. 2019), and externally radiative forcing (Booth et al. 2012; Dunstone et al. 2013; Knudsen et al. 2014; Mann et al. 2021; He et al. 2023).

With respect to the dominant natural variability in the DSPT of the Atlantic Ocean, the Deep Atlantic Multidecadal Variability (DAMV) has been identified and characterized by a north-south dipole pattern between the mid-high latitudes of deep North Atlantic and mid-latitudes of deep South Atlantic with a quasi-periodicity of 20–50 years (Yang et al. 2024). During the positive (negative) phase of the DAMV, the mid-high latitudes of the South Atlantic is filled with a warming (cooling) signal, while the mid-high latitudes of the North Atlantic is dominated by a cooling (warming) signal. Based on the ACCESS ocean model, there is a negative (positive) net meridional OHT in the DAMV north (south) key region during the negative phase, which indicates that more (less) heat is stored in the north (south) key region. Conversely, in the positive phase of the DAMV, more (less) heat is stored in the south (north) key region. Overall, the net OHT driven by the AMOC effectively explains the contrasting changes of deep Atlantic potential temperature in mid-high latitudes, namely the DAMV. To gain a clearer understanding of the AMOC's dynamical role in the vertical structure of the Atlantic Ocean, further investigation of statistical and physical connections between the AMV and DAMV is warranted, considering their similarities in spatial pattern and high temporal correlation.

Extensive research has confirmed that the AMOC facilitates the conveying signals between surface and deep Atlantic. On the one hand, it is well established that the AMOC is capable of transporting surface heat signal to ocean interior (Dickson et al. 2002; Kostov et al. 2014). Recent high-resolution sediment records further demonstrate that the AMOC has integrated and transmitted surface Atlantic variability to the deep ocean over the past 1200 years (Lu et al. 2023). On the other hand, conservation of mass in the ocean implies the existence of compensatory upwelling pathways, particularly in the Southern Ocean and South Atlantic, which likely balance the vertical transport associated with the AMOC (Baker et al. 2025). Recent finding also points out that sub-mesoscale fronts can markedly enhance the upward heat transport from the ocean interior to the surface in the Antarctic circumpolar current (Siegelman et al. 2020), reinforcing the idea that deep Atlantic signals may propagate toward sea surface. Nevertheless, a comprehensive understanding of the coupled transport of heat signals, especially the meridional ocean heat transport, between the surface and deep Atlantic remains elusive. Hence, the AMV and DAMV, as the dominant low frequency variabilities in SST and DSPT in the Atlantic Ocean respectively, are likely to represent a coupled mode of covariability governed by physically coherent dynamics, which offers promising avenues for future research.

2 Data and methods

2.1 Data

This paper utilizes gridded observation deep sea potential temperature data from the EN4 dataset version 4.2.2, which assimilates a diverse range of temperature and salinity observations from the Arctic Synoptic Basin Wide Oceanography project, the Global Temperature and Salinity Profile program, and the Array for Real-time Geostrophic Oceanography project (Good et al. 2013). Recognizing a key limitation of the EN4 dataset that uses climatology in data-sparse regions, the Met Office Statistical Ocean Re-Analysis (MOSORA) is introduced (Smith and Murphy 2007; Smith et al. 2015) to draw a more robust and reliable conclusion, and we use member one of the MOSORA Ensemble (87) in this study. The MOSORA exploits optimal interpolation with long-range covariances to fill the gaps even with sparse observations (Hermanson et al. 2024). The sea surface temperature data are drawn from the NOAA Extended Reconstruction Sea Surface Temperature (ERSST) dataset version 5 and Centennial in situ Observation-Based Estimation Sea Surface Temperature version 2 (COBE) dataset (Hirahara et al. 2014). The ETOPO1 global relief model is used in this study to illustrate the strike of the Mid-Atlantic Ridge.

Apart from the observation and reanalysis datasets, this paper makes good use of model simulations in order to verify the reliability and robustness of conclusions. In order to focus on the natural variabilities of the Atlantic climate system, we introduce the preindustrial control (piControl) simulations in 500 years for GFDL-CM4 and GFDL-ESM4 from the Coupled Model Intercomparison Project Phase 6 (CMIP6) (Eyring et al. 2016). Furthermore, we utilize the past1000 simulation in 1000 years for MRI-ESM2-0 from the Paleoclimate Model Intercomparison Project Phase 4 (PMIP4) considering a longer time span than piControl simulations for comparison. The GFDL-CM4 and MRI-ESM2-0 models show advantages in simulating AMOC variabilities and AMOC cell's geographic structures (Held et al. 2019; Gong et al. 2022). As for the GFDL-ESM4 model, it highlights the improvement of simulating Southern Ocean ventilation and Ocean thermal equilibration compared to the

GFDL-CM4 model, which could contribute to better simulated Antarctic Bottom Water (AABW) production and deep water mass formation (Dunne et al. 2020). All variables are focused on the period from 1950 to 2023, and the global warming signal is removed from all variables by using linear detrending.

2.2 AMV index

The Atlantic Multidecadal Variability index is defined as the detrended average anomalies of sea surface temperatures in the North Atlantic basin typically over 0°–80°N on the basis of the Hadley Centre Global Sea Ice and Sea Surface Temperature (HadISST) version 1.

2.3 DAMV index

Referred to the vertical profile of northward transport in Atlantic basin, Cunningham et al. (2007) indicates that the boundary between upper North Atlantic Deep Water (UNADW) and lower North Atlantic Deep Water (LNADW) is delineated approximately 3000 m. Hence, the Deep Atlantic Multidecadal Variability index is defined as the detrended deep sea potential temperature anomalies averaged over the south key region (25°–40°S, 50°–35°W) subtracted from those over the north key region (45°–60°N, 50°–35°W) based on the EN4 dataset at the depth approximately 3000 m (Yang et al. 2024).

2.4 Singular value decomposition

Singular value decomposition (SVD) is a coupled pattern method used to identify the dominant coupling patterns of variability between two data fields. The SVD method produces two sets of singular vectors and a corresponding set of singular values, which are comparable to the eigenvectors and eigenvalues derived from an empirical orthogonal function analysis, by performing on the temporal cross-covariance matrix of the two fields (Wallace et al. 1992; Lau and Nath 1994; Casey and Adamec 2002). The differences between heterogeneous and homogeneous covariance are calculations and indications: The homogeneous covariance map is determined by the correlations between the A field anomaly values and the expansion coefficient of the A field, which indicates how well the pattern of A anomalies can be specified based on the A anomaly field. To find out that how the pattern of A anomalies can be specified in the B anomaly field, we use the homogeneous covariance map, defined to be the correlations between the A field anomaly values and the expansion coefficient of the B field (Bretherton et al. 1992; Wallace et al. 1992; Casey and Adamec 2002).

2.5 Root mean square skill score (RMSSS)

Root mean square skill score (RMSSS) is a method used to quantify the spatial difference between simulation and observation field that accounts for the spherical effect, adapted from the climatological skill score (An et al. 2024). RMSSS is computed as follows:

$$S = 1 - \frac{E_M}{E} = 1 - \frac{\langle (M_i - O_i)^2 \rangle}{\langle (C_i - O_i)^2 \rangle}, \tag{1}$$

where the angled brackets denote a mean over the n grid points, $E_M = \langle (M_i - O_i)^2 \rangle$ represents the mean square error (MSE) between the simulation and observation, and $E = \langle (C_i - O_i)^2 \rangle$ represents the MSE between the climatology and observation. And $M_i^* = M_i - C_i$ and $O_i^* = O_i - C_i$ donate the anomalies in the simulating and observation fields respectively at the *i-th* grid point.

2.6 Ocean heat transport

Ocean heat transport (OHT) in a certain layer is computed as follows:

$$OHT\,(y,t) = \int_{H_1}^{H_2} \int_{X_{west}}^{X_{east}} v\,(x,y,z,t) \cdot \theta\,(x,y,z,t)\,dxdz \times \rho_0 \times C_p/10^{15}, \tag{2}$$

where C_p is the constant specific heat capacity (4000 J $Kg^{-1}\,K^{-1}$); ρ_0 is the mean density of sea water (1026 kg m^{-3}); H_1 and H_2 are the lower and upper limit of the certain layer; X_{east} and X_{west} stand for the eastern and western boundary; θ is potential temperature; v is meridional velocity.

2.7 Ocean heat transport decomposition

Referred to the standard Reynolds decomposition, the OHT as described in the previous section is referred to as the total OHT, which could be separated into different components induced by mean transport, velocity, temperature, and eddy, respectively (Zhao et al. 2018; Tsubouchi et al. 2021; Wang et al. 2023). In light of the OHT variation based on the low-resolution model simulation, the component driven by mean flow and eddy are not the focus in detail, therefore the OHT driven by velocity and temperature in a certain layer are computed as follows respectively:

$$OHT_{vel}\,(y,t) = \int_{H_1}^{H_2} \int_{X_{west}}^{X_{east}} v'\,(x,y,z,t) \cdot \overline{\theta}\,(x,y,z)\,dxdz \times \rho_0 \times C_p/10^{15}, \tag{3}$$

$$OHT_{temp}(y,t) = \int_{H_1}^{H_2}\int_{X_{west}}^{X_{east}} \theta'(x,y,z,t)\cdot\overline{v}(x,y,z)\,dxdz \times \rho_0 \times C_p/10^{15}, \quad (4)$$

where $\overline{v}(x,y,z)$ is the time average velocity and $\overline{\theta}(x,y,z)$ stands for the time average potential temperature. In consideration of different ocean model grid from CMIP6, it might cause OHT to not always align with constant latitude. Therefore, $v\prime(x,y,z,t)$ and $\theta\prime(x,y,z,t)$ represent deviation from the mean after removing the average velocity and the average potential temperature before calculating the OHT.

2.8 Statistical significance test

In this study, the significance test of correlation is based on the effective sample numbers N_{eff} by the following formula:

$$\frac{1}{N^{\text{eff}}} \approx \frac{1}{N} + \frac{2}{N}\sum_{j=1}^{N-2}\frac{N-j}{N}\rho_{XX}(j)\,\rho_{YY}(j), \quad (5)$$

Here, N is the sample size, ρ_{XX} and ρ_{YY} represent the autocorrelations of the time series X and Y at lag j, individually (Davis 1978; Li et al. 2012; Hao et al. 2025).

3 Results

3.1 A strong coupling between the AMV and DAMV

Given the extensive depth range of deep ocean, this study focuses on the DSPT field at a depth of around 3000 m, which is considered to represent the boundary between upper and lower North Atlantic Deep Water (NADW) (Cunningham et al. 2007). Because the NADW sinks into the deep North Atlantic and flows southward at an approximately depth of 3000 m exhibiting a relatively large gradient of $\delta^{13}C$ in the last glacial period (Marshall and Speer 2012; Kessler et al. 2020; McCarthy et al. 2020), implying that significant DSPT variation is likely to be more detectable near the 3000 m level.

To quantify the coupling between SST and DSPT variability, we apply singular value decomposition (SVD) through identifying linear combinations to have the maximum possible covariance in two geophysical fields (Cherry 1997): the observed SST from the Extended Reconstruction Sea Surface Temperature (ERSST) and observed DSPT from the EN4 dataset. To separate the climate variations from the global warming signal, the SVD analysis is performed on the detrended data by removing a linear fit to the global mean. And we find that the first pair of coupling SVD modes in the observation corresponds well to the spatial patterns of the AMV and DAMV respectively, as Figs. 1 and 2 indicate.

Not only the SVD method but also using the AMV and DAMV classical indices yields AMV–DAMV coupling. As Fig. 1a depicts, the correlation map between AMV index and SST field reveals a basin scale dipole pattern on the whole, with prominent positive anomalies over the North Atlantic and weaker negative anomalies over the South Atlantic and the Atlantic sector of the Southern Ocean. And this dipole pattern closely resembles the AMV-like pattern (Latif et al. 2006; Roberts et al. 2013; Zhang et al. 2013), although incoherent signals emerge in the subpolar North Atlantic and the southwest South Atlantic. In the subpolar North Atlantic, the covariance signal is weakly insignificant positive or even slight negative, in contrast to the widespread significant positive anomalies across the broader North Atlantic. Previous review paper notes a declining linear trend in SST over the subpolar North Atlantic region throughout the past century, a phenomenon commonly referred to as the North Atlantic warming hole (Hansen et al. 2010). The warming hole fingerprint may be due to a slowdown in the AMOC (Rahmstorf et al. 2015). And the reduction of AMOC results in reducing northward heat transport, which is also associated with northward shift of the Gulf Stream based on an ensemble of model simulations from the CMIP5 (Caesar et al. 2018). However, the driving mechanisms remain debated, particularly regarding the contribution of AMOC weakening (Rahmstorf et al. 2015; Hu and Fedorov 2020; Keil et al. 2020; He et al. 2022), which warrants further study from a deep ocean perspective. Regarding to the incoherent positive signal in the southwest South Atlantic is spatially consistent with the South Atlantic Multidecadal Variability, which exhibits the strongest loading over 25°–50°S, 50°–10°W (Xue et al. 2018). Potential mechanisms proposed in previous studies include heat convergence or divergence induced by the South Atlantic Overturning Circulation, as well as nonlinear eddy-mean flow interactions associated with active mesoscale eddies (Le Bars et al. 2016; Lopez et al. 2016). As for spatial pattern for the DSPT, Fig. 1b displays a DAMV-like pattern, characterized by a north-south dipole pattern between the deep North Atlantic mid-high latitudes and deep South Atlantic mid-latitudes (Yang et al. 2024). Significant negative covariance signals are concentrated in the deep North Atlantic, while the positive signals appear in the mid-latitudes of the South Atlantic and the Atlantic sector of Southern Ocean. Overall, the first pair of coupling SVD modes corresponds well to the spatial patterns of the AMV and DAMV via both SVD method and classical indices correlation maps. Both illustrate that the AMV–DAMV coupling is robust across different statistical methods.

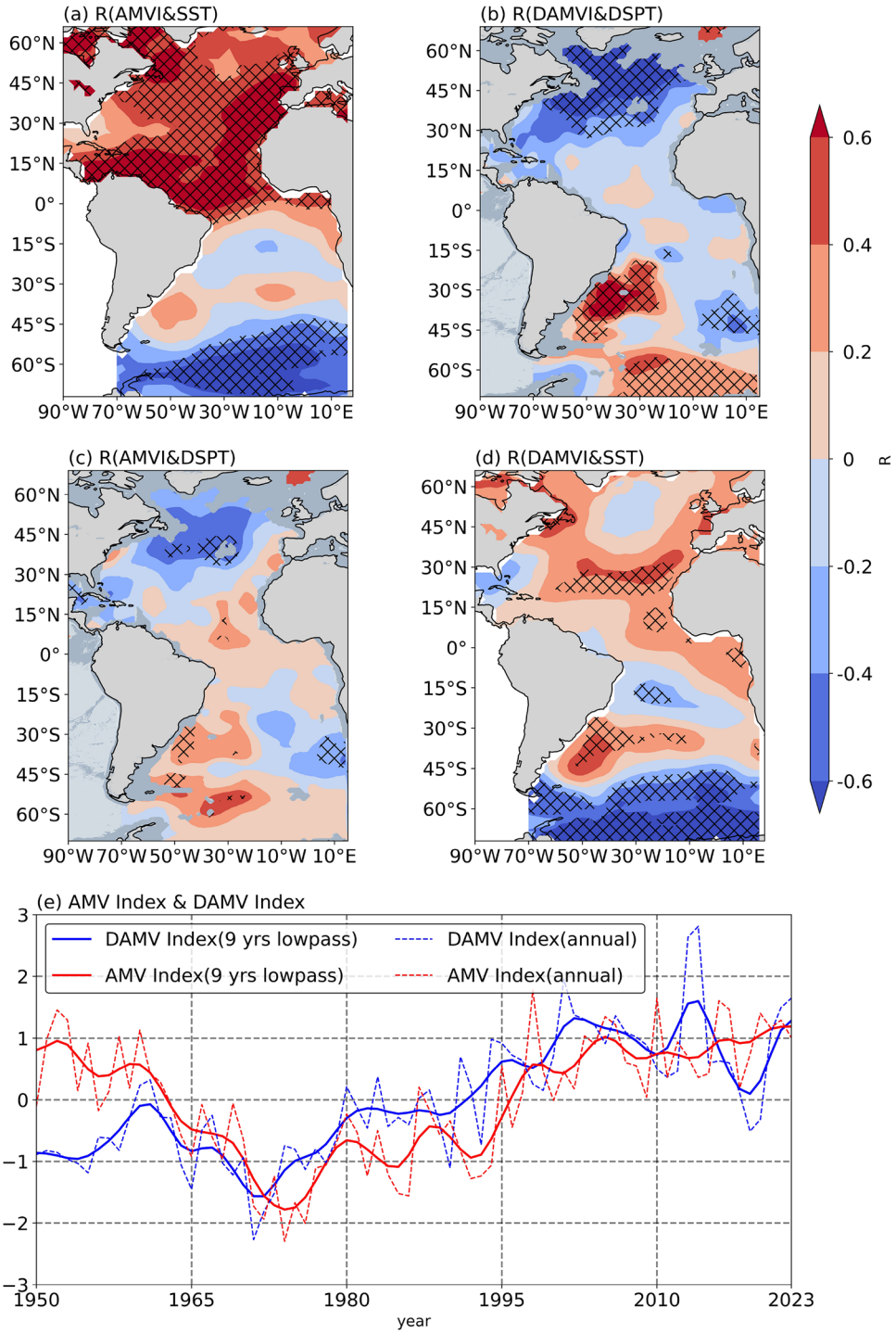

Fig. 1 The coupling between AMV and DAMV based on their own indices. The correlation maps for **a** AMV index and SST, **b** DAMV index and DSPT, **c** AMV index and DSPT, **d** DAMV index and SST. Crosses indicate regions significant at the 95% confidence level based on the effective number of degrees of freedom. Continents are masked in taupe, submarine topography shallower than 3000 m is shaded in gray, and that deeper than 3000 m deep is shaded in dark gray. **e** The annual mean time series of AMV index (dashed red line) and DAMV index (dashed blue line). The 9-year lowpass filtered time series of AMV index (solid red line) and DAMV index (solid blue line)

With respect to temporal behavior, the expansion coefficients for principal component of SVD1 (PC1) for SST and DSPT are strongly correlated with the detrended observed AMV and DAMV indices, with a correlation coefficient of 0.86 (0.95) for AMV (DAMV) index, statistically significant at the 99% confidence level (Fig. 2e). Given the similar spatial patterns of the North Atlantic warming hole and South Atlantic Multidecadal Variability in the SST field, it is necessary to examine their temporal similarities with the expansion coefficients for PC1 for SST. However, the correlation coefficients are merely −0.30 for the North Atlantic warming hole index (Keil et al. 2020), and 0.28 for South Atlantic Multidecadal Variability index (Xue et al. 2018). Taken together, the AMV and DAMV most likely represent the first dominant SVD mode between the SST and DSPT

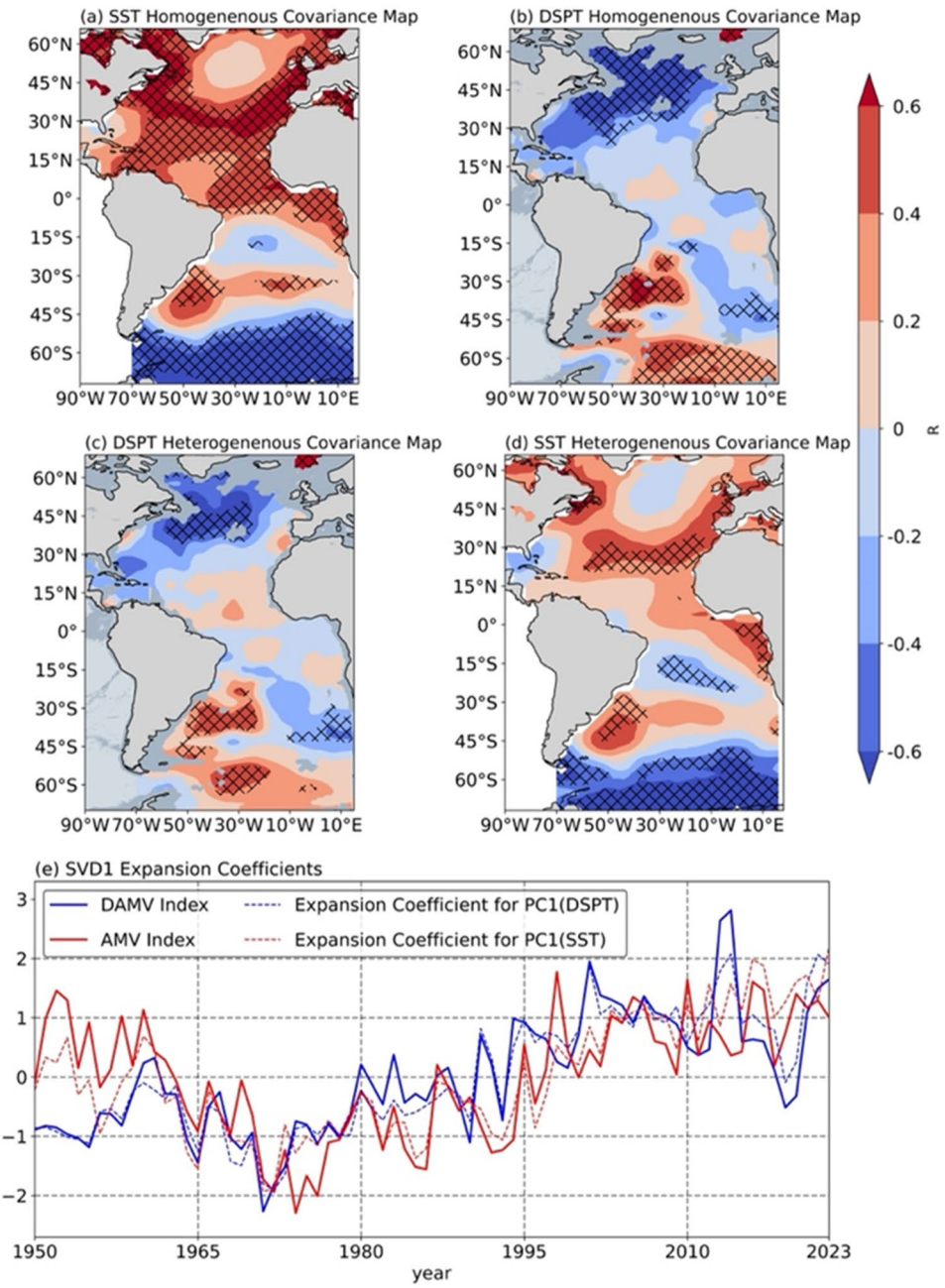

Fig. 2 The leading SVD1 mode of the covariance between the SST and DSPT in the Atlantic Ocean derived from observation. The homogeneous covariance maps for **a** SST and **b** DSPT, along with the heterogeneous covariance maps for **c** SST and **d** DSPT. Crosses indicate regions significant at the 95% confidence level based on the effective number of degrees of freedom. Continents are masked in taupe, submarine topography shallower than 3000 m is shaded in gray, and that deeper than 3000 m deep is shaded in dark gray. **e** The annual mean time series of normalized expansion coefficients for principal component of SVD1 (PC1) of SST (dashed red line), PC1 of DSPT (dashed blue line), the AMV index (solid red line), and the DAMV index (solid blue line). The SVD1 mode accounts for 27.37% of the squared covariance fraction (SCF)

in the Atlantic Ocean, considering both spatial pattern and temporal behavior simultaneously.

Notably, the coupling between the AMV and DAMV is found to be statistically strong. Three lines of statistical evidence as supported above-mentioned conclusion: Firstly, the leading SVD1 accounts for 27.37% of the squared covariance fraction (SCF), and is significant at the 95% confidence level based on the Monte Carlo significance test (Wallace et al. 1992). Secondly, the expansion coefficients for PC1 are highly correlated of 0.78, which is significant at the 95% confidence level using the large-lag standard error method (Casey and Adamec 2002). Thirdly, the SST (DSPT) heterogeneous covariance maps closely resemble the DSPT (SST) homogeneous covariance maps respectively (Fig. 2a–d). On the one hand, this correspondence illustrates that the influence of the AMV on the DSPT field manifests a DAMV-like pattern (Fig. 1c), demonstrating a high degree of similarity with Fig. 1b in the spatial pattern. Pronounced negative loadings are predominantly localized over the mid-to-high latitudes of the deep North Atlantic, while significant positive signals emerge in the mid-latitudes of the deep South Atlantic and the Atlantic sector of the Southern Ocean (Yang et al. 2024). On the other hand, the influence of DAMV on the SST field exhibits an AMV-like

pattern (Fig. 1d), similar to the Fig. 1a. In brief, the dominant SVD1 reveals a statistically strong coupling between the AMV and DAMV with high probability in observation.

In order to ensure that there is a robust and continuous AMV–DAMV coupling signal at some depths range connecting surface and deep Atlantic, the correlation maps between AMV (DAMV) indices and the average DSPT from 2500 to 3500 m are applied. As Fig. S1 shows, it also displays the AMV–DAMV coupling in spatial–temporal behaviors, which is highly consistent with the Fig. 1 on the whole. In details, we also show the SVD1 results derived from every adjacent depth from 2500 to 3500 m for the sake of enhancing the robustness of the observed strong coupling between AMV and DAMV. The spatial patterns of SVD1 for SST and DSPT at these layers show a high degree of similarity with AMV and DAMV (Fig. 3a–h). All the correlation coefficients between the expansion coefficients for PC1 in the SST (DSPT) and the detrended observed AMV (DAMV) indices exceed 0.8 and are statistically significant at the 99% confidence level (Supplementary Table S1). The average SCF explained by the SVD1 at these depths is 24.66% and the average correlation coefficient between the expansion coefficients for SST and DSPT is 0.76 (Supplementary Table S1). Therefore, these provide collateral evidence that the strong coupling between AMV and DAMV across adjacent layers evidently persists, further proving the reliability and robustness of DAMV in a coupled perspective.

Considering the accelerated warming rate of the North Atlantic average SST, removing a quadratic trend provides a significantly better fit than a linear trend for modeling AMV (Zanchettin and Rubino 2024). To determine whether the AMV–DAMV coupling is independent on the method of global warming signal removing, this study also reproduces the SVD analysis after removing quadratic fit of both SST and DSPT field. As Fig. S2 indicates, we find that the AMV–DAMV coupling still shows up after removing quadratic trend, indicating that the above-mentioned AMV–DAMV coupling is robust across different detrend methods as well.

Nonetheless, the SST and DSPT fields from the observation are limited in temporal coverage, which constrains their utility in investigating multidecadal variability. Moreover, the observational uncertainties, particularly in the DSPT dataset, are nonnegligible. To strengthen the robustness of the identified strong coupling between the AMV and DAMV, we additionally utilize the state-of-art DSPT reanalysis data from the Met Office Statistical Ocean Re-Analysis (MOSORA), and multi-model data from distinctive simulation experiments, including the 500-year preindustrial control (piControl) simulations for GFDL-CM4 and GFDL-ESM4 from the Coupled Model Intercomparison Project Phase 6 (CMIP6), as well as the 1000-year past1000 simulation for MRI-ESM2-0 provided by the Paleoclimate Model Intercomparison Project Phase 4 (Eyring et al. 2016).

The dominant SVD1 derived from reanalysis is extracted from the Centennial in situ Observation-Based Estimates Sea Surface Temperature version 2 (COBE) (Hirahara et al. 2014) and MOSORA datasets (Smith and Murphy 2007; Smith et al. 2015). The homogeneous covariance maps for SST and DSPT reveal an AMV–DAMV coupling pattern, resembles the spatial patterns identified in the observation (Fig. 4a–b). Considering that qualitative descriptions of similarities and disparities in the spatial–temporal features across the three models tend to lack intuitive clarity, we employ the root mean square skill score (RMSSS) to quantitatively assess the spatial differences (An et al. 2024), as well as the correlation analysis and power spectrum to provide a more straightforward way to quantify the temporal similarity. From the perspective of spatial pattern, the RMSSS is 0.55 (0.36) for the AMV-like pattern in the SST field (DAMV-like pattern in the DSPT field). Both are above 0, demonstrating that the reanalysis captures a majority of spatial features associated with the AMV and represents those of the DAMV. In terms of temporal behavior, the expansion coefficients for PC1 of SST and DSPT exhibit a significant correlation with the detrended AMV and DAMV indices, with correlation coefficients of 0.86 and 0.77 respectively, both significant at the 99% confidence level using the effective number of degrees of freedom, which indicates that the reanalysis catches the main temporal features of AMV and DAMV. According to the power spectrum, the expansion coefficients for PC1 of SST exhibit a significant band on the multidecadal timescale spanning 20–60 years, closely matching the spectral features of the AMV (Gulev et al. 2013; Tung and Zhou 2013; Borchert et al. 2018). Similarly, the PC1 for DSPT highlights a pronounced quasi-periodic signal between 20 and 50 years, consistent with the spectral features of DAMV (Yang et al. 2024). Overall, the SVD1 results from the reanalysis exhibit an AMV–DAMV coupling as well, showing a high degree of similarity with the observation results quantitatively.

In order to distinguish basic AMV and DAMV signals across different model simulations, it is necessary to quantify the similarity via the RMSSS, correlation analysis and power spectrum. As for the spatial similarity, all RMSSS values are positive, except for the AMV pattern in GFDL-CM4, indicating that all three models generally have reasonable spatial simulation skills of both AMV and DAMV simultaneously (Table 1). Although the RMSSS for the AMV pattern in GFDL-CM4 is −0.09, it still captures a robust positive signal over the North Atlantic, which has been identified as a key region to the AMV due to its strongest loadings (Enfield et al. 2001; Deser et al. 2010; Knudsen et al. 2011). On the contrary, MRI-ESM2-0 shows the highest

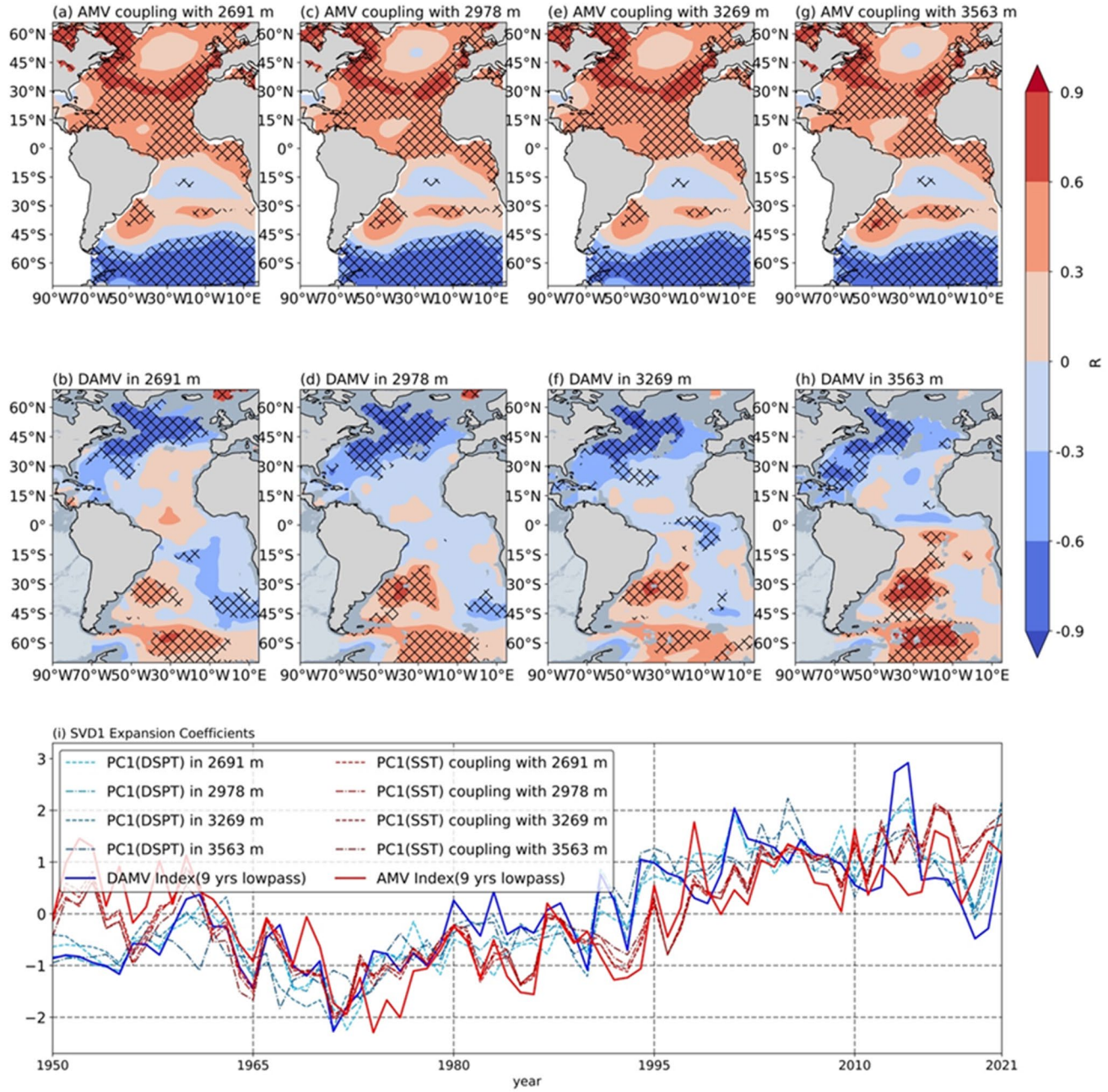

Fig. 3 The leading SVD1 mode between SST and DSPT in close layers at the depths spanning from 2500 to 3500 m in observation. The homogeneous covariance maps for SST coupling with **a** 2691 m, **c** 2978 m, **e** 3269 m, and **g** 3563m. And (**b**), (**d**), (**f**), and (**h**) are the same, but for DSPT in close layer around 3000 m. Crosses indicate regions significant at the 95% confidence level based on the effective number of degrees of freedom. Continents are masked in taupe, submarine topography shallower than 3000 m is shaded in gray, and that deeper than 3000 m deep is shaded in dark gray. **i** The 9-year lowpass filtered time series of normalized expansion coefficients for PC1 of SST (red lines), PC1 of DSPT (blue lines), the AMV index (dashed red line), and the DAMV index (dashed blue line). The average of SVD1 mode accounts for 24.66% of the squared covariance fraction

skill in reproducing the observed AMV–DAMV coupling, with the RMSSS of 0.07 and 0.39, which even exceeds the value obtained from reanalysis. Yet, this model underestimates SST variability in the South Atlantic and the Atlantic sector of the Southern Ocean, which may partially explain its high RMSSS. Previous papers point out that substantial SST biases in the South Atlantic Ocean and Southern Ocean have persisted across multiple generations of CMIP models, possibly associated with the AMOC strength in CMIP5 models (Wang et al. 2014), and linked to common biases in the deep North Atlantic transported adiabatically related to

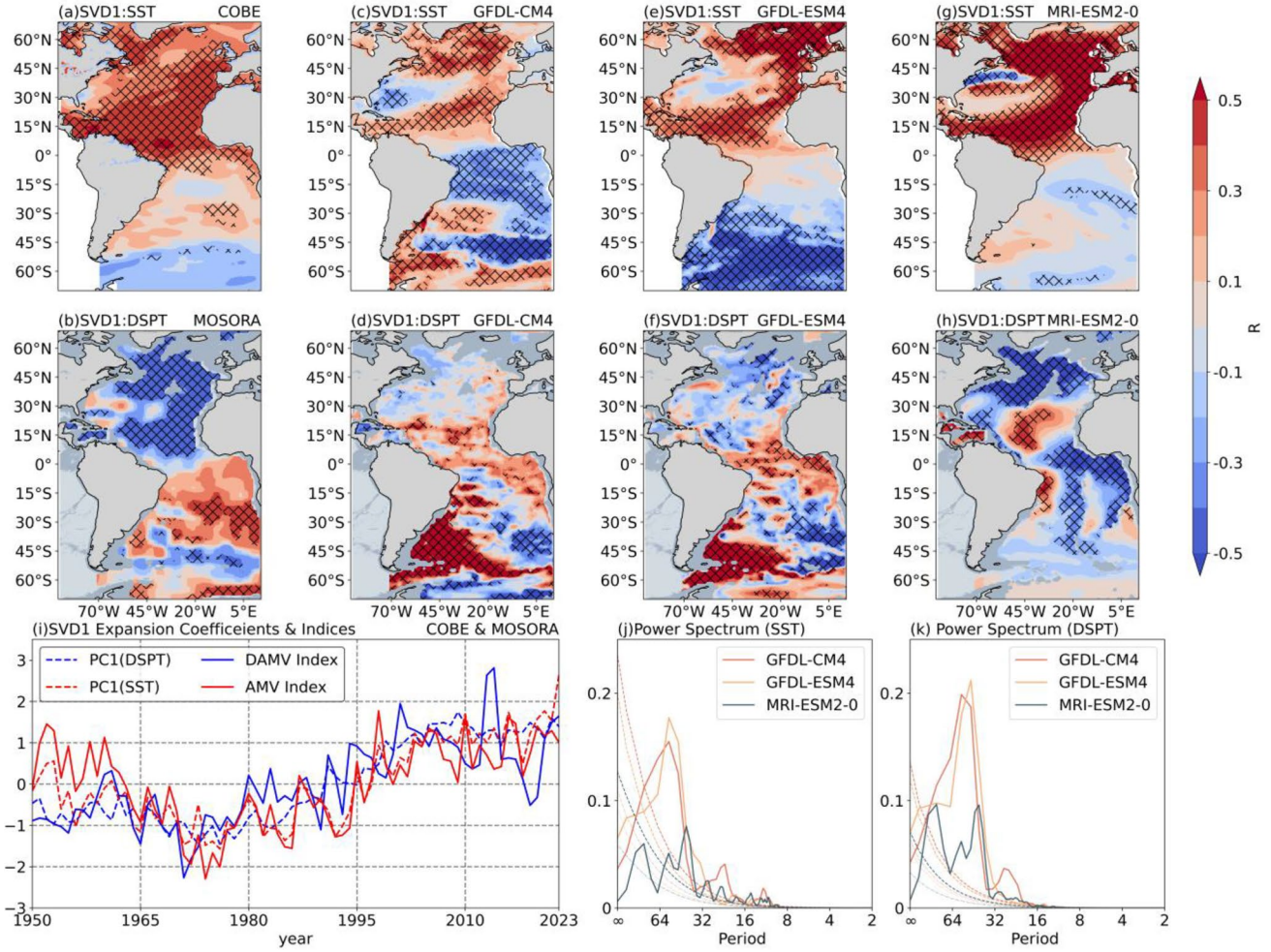

Fig. 4 The leading SVD1 mode between the SST and DSPT in the Atlantic Ocean from reanalysis and multi-model simulations. The homogeneous covariance maps for SST from **a** The Centennial in situ Observation-Based Estimates Sea Surface Temperature version 2 (COBE) dataset, **c** GFDL-CM4, **e** GFDL-ESM4, and **g** MRI-ESM2-0. **b** The homogeneous covariance maps for DSPT from MOSORA dataset. **d**, **f**, and **h** present the corresponding DSPT homogeneous maps for GFDL-CM4, GFDL-ESM4, and MRI-ESM2-0 respectively. Crosses indicate regions significant at the 95% confidence level based on the effective number of degrees of freedom. Continents are masked in taupe, submarine topography shallower than 3000 m is shaded in gray, and that deeper than 3000 m deep is shaded in dark gray. **i** The annual mean time series of normalized expansion coefficients for PC1 of SST (dashed red line), DSPT (dashed blue line), observed AMV index (solid red line) and observed DAMV index (solid blue line). **j** Power spectrum of the 9-year lowpass filtered PC1 of SST from GFDL-CM4 (orange), GFDL-ESM4 (yellow), and MRI-ESM2-0 (dark green). **k** The same as (**j**), but for the 9-year lowpass filtered PC1 of DSPT. In (**j**–**k**), the dashed lines are the 95% significance level corresponding to the red noise spectrum, and the dot-dashed lines are red noise line

Table 1 Spatial and temporal similarities of the leading SVD1 from multi-model simulations

Datasets	Spatial pattern	RMSSS	R (PC1, Index)	Power spectrum	SCF (%)	R
GFDL-ESM4	AMV-like	0.09	0.75*	40–80 years	21.37	0.83*
	DAMV-like	0.02	0.53*	20–80 years		
GFDL-CM4	AMV-like	−0.09	0.29	30–70 years	17.04	0.86*
	DAMV-like	0.03	0.84*	20–90 years		
MRI-ESM2-0	AMV-like	0.39	0.70*	30–60 years	33.71	0.71*
	DAMV-like	0.07	0.73*	20–80 years		

In the third column, the RMSSS is calculated between AMV (DAMV) pattern and SST (DSPT) spatial pattern of SVD1 distinctively. In the fourth column, index in SST (DSPT) field stand for the AMV (DAMV) index derived from the observation. As for the fifth column, it summarizes the significant quasi-periodicity of the 9-year lowpass filtered the expansion coefficients for PC1 of SST and DSPT field separately, which is significant at the 95% significance level corresponding to the red noise spectrum. And asterisk (*) indicates that the correlation coefficients are statistically significant at the 95% confidence level based on the effective number of degrees of freedom

ocean process by the AMOC in CMIP6 models (Luo et al. 2023).

To initially identify the presence of AMV and DAMV signals in temporal aspects, we perform correlation analysis between the expansion coefficients for PC1 and their indices. It is found that all the significant correlation coefficients exceed 0.5, apart from the SST signal for GFDL-CM4. It suggests that the multi-model simulations are capable of reproducing coupling of the AMV and DAMV via the SVD method. And power spectrum analysis reveals a significant peak spanning 30–70 years approximately for the expansion coefficients for PC1 in SST field, and a generally significant band between 20 and 80 years in the DSPT field with subtle discrepancies (Fig. 4j–k). This broader spectral range not only validates the coupling of AMV and DAMV by exhibiting close spectral characteristics, but also illustrates that the present observational record may be insufficient to fully capture multidecadal variability indeed (Kravtsov et al. 2014; Steinman et al. 2015). In addition, consistently significant correlations between the expansion coefficients for PC1 further confirm their robust coupling across the multi-model simulations.

Moreover, based on the AMV sub-ensemble proposed by Zanchettin and Rubino (2024), which is the sub-ensemble with simulations most realistically representing the observed AMV from historical simulations in the CMIP6. As Table S2 shows, this study uses 11 models consistent with the AMV sub-ensemble, and picks up the best simulating run for each model in representing the AMV and DAMV conjointly. And the AMV–DAMV coupling could be obtained via the SVD analysis based on the AMV sub-ensemble (Fig. S3), further validating that the AMV and DAMV are coupling derived from a variety of model simulations.

To summarize, despite minor quantitative distinctions in spatiotemporal features, the leading SVD1 consistently reveals a robust and strong coupling interaction between the AMV and DAMV across different types of model simulations. As the dominant coupling modes of SST and DSPT in the Atlantic Ocean, AMV and DAMV are separated by a vertical depth difference of approximately 3000 m, while the AMOC acts as one of the coupled dynamical mechanisms underlying both variabilities. Hence, apart from the strong coupling, their potential lead-lag relationship remains an open question requiring further investigation.

3.2 Lead-lag correlations of the AMV and DAMV

Recent research has revealed a significant synchronous correlation between the AMV and DAMV, with a correlation coefficient of 0.60 based on the 9-year lowpass filtered observational data (Yang et al. 2024). Referred to temporal evolution of the AMV and DAMV indices, it is plausible that a time delay relation exists, which deserves to be further investigated among observation, reanalysis, and multi-model simulations.

Figure 5a illustrates the lead-lag correlation between the AMV and DAMV indices in observation represented in red, as well as reanalysis shown in blue. As for the observation result, a positive correlation is observed when the DAMV leads the AMV, whereas a negative correlation appears when then DAMV lags AMV. More precisely, the DAMV leads AMV by approximately 0–26 years, with a pronounced peak at a 7-year lead, where the lead correlation coefficient reaches 0.76. The DAMV leads AMV by 1 or 2 decades, and such leading correlation aligns with the timescale of water mass transport driven by deep convection, typically spanning a decade or even longer (Curry et al. 1998; Rhein et al. 2015; Buckley and Marshall 2016). Conversely, the DAMV lags AMV by roughly 18–35 years, with the strongest negative correlation coefficient of −0.92 when lagging 30 years. Given a longer time delay about the DAMV lagging AMV, it is inclined to demonstrate that signals from the deep Atlantic take 2 or 3 decades to reach the sea surface in the South Atlantic and the Atlantic sector of the Southern Ocean. And it is coincident with previous results indicating that NADW at depths of 1000–3500 m takes several decades to upwell from 30°S to the surface mixed layer by Lagrangian upwelling particle transport (Tamsitt et al. 2017). Moreover, the reanalysis shown in blue sheds light on that both lead and lag correlations are robust between the AMV and DAMV (Fig. 5a). In order to draw a robust lead-lag correlation between AMV and DAMV at the adjacent layers around 3000 m, Figure S4 and Table S3 show that the above-mentioned time-delayed relationship between AMV and DAMV from 2500 to 3500 m is significantly robust, consequently leading to that it is independent to the chosen layer of DAMV. However, since the observation and reanalysis data span merely 74 years, conclusions regarding the DAMV lagging AMV by approximately 30-year should be interpreted with caution.

As for spatial aspect, Fig. 6a–b shows the leading (lagging) influence of DAMV on the SST field when DAMV leading (lagging) 7 (30) years, which are consistent with the lead-lag correlation peaks between AMV and DAMV. Figure 6a shows high degree of similarity with Fig. 1d, with the strong and significant positive loadings mainly center on the North Atlantic, apart from the warming hole region and the Southwest North Atlantic. It is predominantly associated with the positive phase of AMV, which is well-matched with the positive correlation when DAMV leads AMV 7 years. Regarding the DAMV lagging AMV, Fig. 6b exhibits the lagging influence of DAMV on the SST field, with the strongest negative loadings filling with the North Atlantic, apart from the warming hole region. This pattern

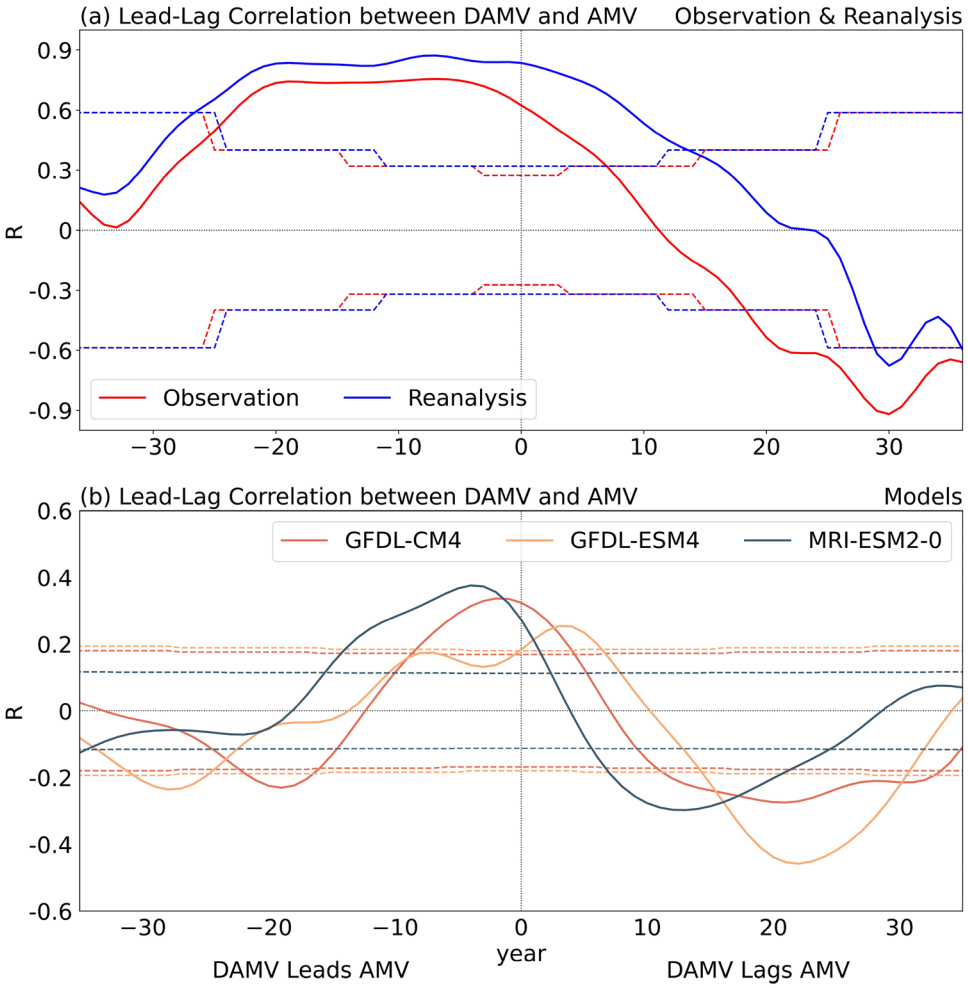

Fig. 5 The lead-lag correlation between the AMV and DAMV from observation, reanalysis and multi-model simulations. **a** Lead-lag correlation between detrended annual mean DAMVI and AMVI (1950–2023) after 9-year Gaussian low-pass filtering in observation (red) and reanalysis (blue). Dashed lines denote the 85% confidence levels using the effective number of degrees of freedom. **b** The same as (**a**), but for the GFDL-CM4 (orange) in 500 years, GFDL-ESM4 (yellow) in 500 years, and MRI-ESM2-0 (dark green) in 1000 years. Dashed lines denote the 90% confidence levels using the effective number of degrees of freedom

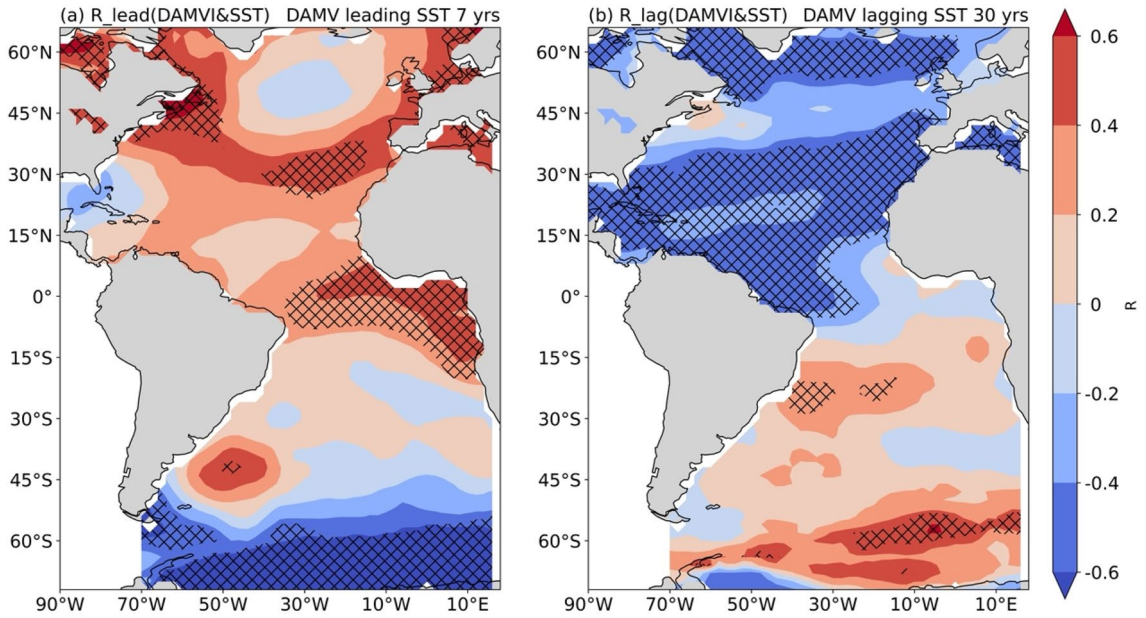

Fig. 6 Lead-lag correlation maps between the DAMV and SST field. **a** The lead correlation map about the DAMV index leading the SST anomaly 7 years. **b** The lag correlation map about the DAMV index lagging the SST anomaly 30 years. The areas marked by crosses are significant at the 95% confidence level

is consistent with the negative phase of AMV, which is also matched with the negative correlation when DAMV lags AMV 30 years. Hence, the leading (lagging) influence of DAMV on SST exhibits positive (negative) phase of AMV in spatial pattern, which indicates that the DAMV could be served as a deep-ocean fingerprint to connect the AMV phase transition from the perspective of spatial pattern.

To further assess the robustness of the time delay relationship between the AMV and DAMV, the multi-model simulations over longer time spans are analyzed. As shown in Fig. 5b, the DAMV leads AMV by 1 decade approximately, with statistically significant peak correlation coefficient of 0.34 for GFDL-CM4 and 0.38 for MRI-ESM2-0 (Table 2). Although GFDL-ESM4 does not exhibit a significant lead correlation, its maximum correlation also occurs when the DAMV leads AMV by 7 years, consistent with the other model simulations. In addition, the DAMV commonly lags AMV by around 2 decades, which is shorter than the observation and reanalysis (Table 2). Combined with the observation, reanalysis and multi-model simulations, all consistently suggest that the lead-lag correlations of the AMV and DAMV is characterized by a positive lead correlation (DAMV leading AMV) by roughly 1 decade and a negative correlation (DAMV lagging AMV) by nearly 2 or 3 decades.

Furthermore, above-mentioned results naturally raise the surmise of whether strong coupling and lead-lag correlations between AMV and DAMV can coexist simultaneously. To explore this, the present study examines the correlation maps between the DAMV index and Atlantic zonal mean sea potential temperature at different time lags, corresponding to the time delay of AMV and DAMV in sequence. It reveals a robust multidecadal cycle composed of a positive DAMV signal at lag 0 year, a positive AMV signal at lag around 5 years, a negative DAMV at lag around 35 years, and a negative AMV at lag around 40 years (Supplementary Fig. S5a–m). Overall, it identifies the simultaneous presence of strong coupling and lead–lag correlations between AMV and DAMV in the Atlantic zonal-mean sea potential temperature profile, and is found to be mutually compatible, particularly in the context of multi-model simulations.

Preceding papers evaluate the lead-lag correlations of the AMV and AMOC, demonstrating that the majority of models reproduce a positive (negative) correlation when the AMOC leads (lags) AMV in CMIP5 models (Zhang and Wang 2013), which aligns with the delayed advective oscillation mechanism (Lee and Wang 2010). And such lead-lag correlation between AMV and AMOC is consistent and robust, based on the two large ensembles for CESM and IPSL (Frankignoul et al. 2017) and five different AMOC indicators (Sun et al. 2021). Besides, the lead-lag correlation of the DAMV and AMOC is established based on the ocean model, revealing that the AMOC leads (lags) DAMV by 13 (16) years roughly (Yang et al. 2024). And it is found that both AMV and DAMV exhibit a lead-lag relationship with AMOC, implying that physical dynamics mechanism underlying the coupling and time delay correlation of the AMV and DAMV is likely to have a potential association with the AMOC.

3.3 Ocean heat transport in AMV-related and DAMV-related regions

To establish the dynamic role of the AMOC in AMV–DAMV delayed coupling, OHT is calculated based on GFDL-CM4 and MRI-ESM2-0 in this study, due to the unavailability of meridional velocity and weakest simulating skills in the AMV–DAMV lead-lag relationship for GFDL-ESM4 among these three models. Furthermore, GFDL-CM4 displays superior skills in simulating the delayed coupling between the AMV and DAMV, compared to the MRI-ESM2-0. Therefore, OHT results from GFDL-CM4 are presented in the main text, whereas the results from MRI-ESM2-0 are provided as supporting evidence. Referred to the robustness of coupling between AMV and DAMV in close layers, OHT is calculated within upper 200 m to represent the surface OHT, and at the depths from 2500 and 3500 m to represent the deep OHT.

As Fig. 7a depicts, time series of net total OHT in AMV-related regions exhibit alternating positive and negative phases on multidecadal timescales jointly. Notably, during most of the 500-year period, net OHT in north key region of the AMV shown in red bars is positive when that in south key region is negative in blue bars, and vice versa. This out-of-phase relationship aligns with the north–south dipole pattern of the AMV over the Atlantic Ocean. While the AMOC

Table 2 The lead-lag correlation results between the DAMV and AMV among observation, reanalysis, and multi-model simulations

Datasets	Leading years	R_{max}	Leading year of maximum	Lagging years	R_{min}	Lagging year of minimum
Observation	26–0	0.75**	7	28–32	−0.91**	30
Reanalysis	22–0	0.87**	7	26–35	−0.71**	30
GFDL-ESM4		0.25	7	15–28	−0.46**	22
GFDL-CM4	8–0	0.34*	2	18–22	−0.27*	21
MRI-ESM2-0	15–0	0.38*	4	7–22	−0.30*	13

Asterisk (*) and double asterisk (**) represent the correlation coefficients are significant at the 85% and 90% respectively, confidence level based on the effective number of degrees of freedom

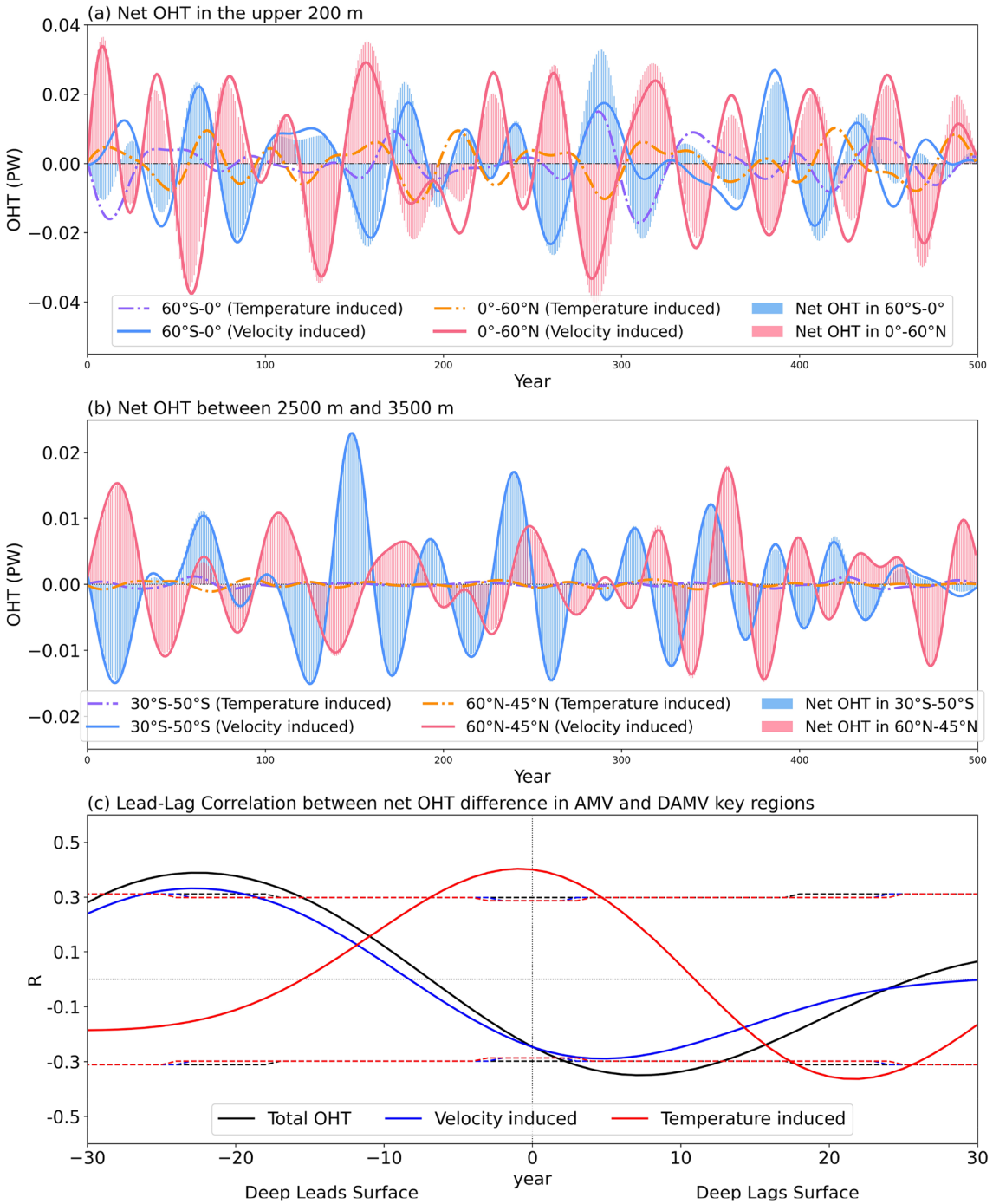

Fig. 7 Temporal features of net meridional ocean heat transport in AMV and DAMV key regions for GFDL-CM4. Net meridional ocean heat transport (units: PW) in **a** two key regions of AMV in the upper 200 m (north: 0°–60°N, south: 60°S–0°), and **b** two key regions of DAMV between 2500 and 3500 m (north: 45°–60°N, south: 30°–50°S). In (**a**–**b**), red bars represent the total OHT in north key regions decomposed into temperature-induced component in orange dash-dotted lines and velocity-induced component in red solid lines, while blue bars stand for the total part in south key regions, and purple dash-dotted lines (blue solid lines) represent temperature-induced component (velocity-induced component). **c** Lead-lag correlation between net meridional ocean heat transport in the AMV North Atlantic region and the ocean heat transport difference between two DAMV key regions for total OHT in black, velocity-induced component in blue, and temperature-induced component in red. Dashed lines denote the 85% confidence levels using the effective number of degrees of freedom. In (**a**–**c**), a 29–99 years Butterworth band-pass filter is applied to focus on the multidecadal variability

variability on interannual timescale is predominantly driven by local wind-forced Ekman transport (Hirschi and Marotzke 2007; Kanzow et al. 2007), its decadal variability reflects a complex interaction between wind-driven and thermohaline processes (Böning et al. 2006; Yeager and Danabasoglu 2014; Buckley and Marshall 2016). It demonstrates that net total OHT in AMV-related regions exhibits both the spatial features and temporal behaviors of the AMV, implying possible dynamic driver role of the AMOC in modulating AMV to a certain extent (Zhang 2010; Delworth and Zeng 2012; Schmith et al. 2014). According to the OHT decomposition method, the total OHT could be decomposed into temperature-induced component and velocity-induced component (Zhao et al. 2018; Tsubouchi et al. 2021). The contributions of the velocity-induced component for north (south) key region of the AMV shown in red (blue) solid line, are both significantly larger than the temperature-induced component in orange (purple) dash-dotted line. Prior research finds that the northward meridional OHT in the Atlantic Ocean is primarily driven by velocity-driven component with large discrepancies between CMIP5 and CMIP6 (Mecking and Drijfhout 2023). Therefore, the OHT variability in the upper 200 m mainly driven by velocity variation may serve as a key dynamical contributor to AMV.

Likewise, time series of net total OHT in DAMV-related regions display synchronized multidecadal oscillations between positive and negative phases, reproducing the essential spatiotemporal characteristics of the DAMV (Fig. 7b). In the north (south) key region of the DAMV, the velocity-induced components overwhelmingly dominate the total OHT, exceeding the temperature-induced components by an order of magnitude. Compared to the surface OHT, the velocity variation in the deep Atlantic plays an irreplaceable role in the OHT, further underscoring the key role of the AMOC in the deep Atlantic Ocean. Drawing upon high concentrations of Chlorofluorocarbon, which are commonly used to estimate age of the NADW, previous study reveals that NADW propagate to 20°S in the deep southwest South Atlantic within 30 years approximately, and further demonstrates that its dynamical mechanisms involving advection in the Deep Western Boundary Current, recirculation within deep gyres, and mixing processes (Smethie et al. 2000; Fine et al. 2002; Rhein et al. 2015). Considering the fundamental role of NADW in shaping the DAMV key regions, the estimated 30-year advective timescale for NADW from the north key region to the south one is temporally consistent with multidecadal changes of the DAMV. Therefore, the DAMV is likely modulated primarily by velocity-induced OHT in the deep Atlantic between 2500 and 3500 m.

In summary, the AMV and DAMV can be primarily attributed to the OHT in the surface and deep Atlantic, with both being mainly induced by velocity variation. However, evidence from OHT fluctuations remains quantitatively insufficient, particularly in providing robust proof regarding their time delay features. Naturally, this raises the question of whether corresponding lead-lag correlation are present in their associated OHT result.

To further validate the role of AMOC in the delayed coupling between AMV and DAMV, Fig. 7c quantifies the statistical temporal similarities through lead-lag correlation. Figure 7c depicts that a positive correlation occurs when deep OHT leads surface OHT, which reverses to a negative correlation when deep OHT lags. This time delay features remarkably resemble the lead-lag correlation of the AMV and DAMV depicted in Fig. 5. Specifically, the total deep OHT in black line leads surface total OHT by approximately 16–28 years, with a significant maximum correlation of 0.39 occurring at a 23-year lead. Conversely, the negative deep OHT lags surface OHT by roughly 3–14 years, and the lag correlation coefficient reaches a peak of −0.38 when deep lagging surface by 7 years. Likewise, due to velocity-induced component prevailing in the total OHT, an analogous lead-lag correlation is found in the velocity-induced component in blue line. However, the lead-lag correlation of both the total OHT and its velocity-induced component differs substantially from the distinct time delay features observed in the AMV–DAMV relationship. This suggests that velocity-induced component, despite being the primary driver of total OHT variations, appears to play a limited role in generating the observed time delay in AMV–DAMV coupling.

On the contrary, as Fig. 7c red line indicates, temperature-induced component in deep Atlantic Ocean leads it of surface OHT by approximately 0–7 years, with a prominent positive peak reaching 0.40 at a 1-year lead. And the deep OHT induced by temperature lags temperature-induced component in surface Atlantic Ocean by roughly 17–26 years with the greatest lag correlation coefficient of −0.36 when lagging 22 years. It could be characterized by a positive correlation when temperature-induced deep OHT leads it in surface OHT by 1 decade approximately and a negative correlation when lagging by around 2 decades. Hence, the temperature-induced component of OHT associated with the AMV and DAMV is congruent with that of AMV and DAMV, indicating that OHT driven by temperature variation can provide an effective explanation for the time delay feature between AMV and DAMV, in spite of contributing less to the total OHT compared with the velocity-induced component.

To ensure the robustness of the decomposed OHT components and their relative contributions to the delayed coupling between AMV and DAMV, the MRI-ESM2-0 results are calculated as well. Although the temperature-induced component accounts for only a small fraction of the total

OHT, it plays a pivotal role in the lead-lag relationship between AMV and DAMV, exhibiting a more pronounced and consistent lead-lag relationship than the velocity-induced component (Supplementary Fig. S6). In general, both surface and deep OHT effectively capture the primary spatiotemporal characteristics of AMV and DAMV conjointly. Their lead-lag correlation is primarily governed by the temperature-induced component of the total OHT, reinforcing the rationale for constructing OHT driven by the AMOC as a physical mechanism for the delayed coupling between AMV and DAMV.

4 Discussion

This study reveals a statistically robust and physically coherent coupling between the AMV and DAMV, suggesting that the DAMV likely represents a deep-ocean symbiotic fingerprint of the AMV. Among the observation, reanalysis and multi-model simulations, we identify a dominant coupled mode characterized by a basin scale dipole pattern in SST resembling the AMV pattern, accompanied by a DAMV-like dipole pattern in DSPT field over the mid-to-high latitudes of the Atlantic Ocean. The strong correlations between the expansion coefficients of the SVD1 and AMV (DAMV) indices separately further confirm the coupling of AMV and DAMV in temporal behavior. Owing to the high SCF of SVD1, strong correlation between the expansion coefficients for PC1, and the heterogeneous covariance maps, the strong influence of AMV (DAMV) on the DSPT (SST) field displays a DAMV (AMV) pattern mutually, demonstrating that the dominant SVD1 captures a pronounced coupling interaction between the AMV and DAMV.

More importantly, this study uncovers a remarkable lead-lag relationship between AMV and DAMV, with DAMV leading AMV by approximately 1 decade and lagging by 2 to 3 decades, as supported by observational, reanalysis, and multi-model simulation evidence. Given the shortage in time span of deep-sea observation dataset, using the multi-period ensemble mean from model simulations divided in the same time span as the observation shows that the AMV–DAMV lead-lag relationship derived from the multi-period ensemble mean is highly similar to it from the entire time span (Fig. S7). It proves that the discrepancies in AMV–DAMV delayed relationship between observations and model simulations primarily due to model biases, and possibly affected by the sample size, particularly in the significance of lead-lag correlation.

Through OHT analysis, both surface and deep OHT exhibit spatial patterns and temporal behaviors that qualitatively resemble those of the AMV and DAMV, respectively. Furthermore, the lead-lag correlations of the temperature-induced OHT between AMV-related and DAMV-related regions mirror that between the AMV and DAMV indices, albeit accounting for a relatively small fraction of total OHT variability. This supports the interpretation of AMOC-driven OHT as a plausible physical interpretation underlying the delayed coupling between AMV and DAMV, while the direct physical mechanism needs further investigation via dynamical method. Given the possible discrepancy between AMOC and ocean transports, the meridional transports in both UNADW and LNADW layers are linked to local AMOC at subpolar latitudes, yet only LNADW transport shows linkage to AMOC in the subtropical gyre (Zou et al. 2019). And the deep OHT calculating within 2500 m and 3500 m in this study is well-matched with such AMOC-meridional transports coherency in the LNADW layers, indicating that previous paper corroborates our results. In particular, the southward transport in deep Atlantic at 8°S is exclusively mediated by propagating eddies, as direct velocity measurements reveal an absence of persistent mean flow within the NADW layer (Dengler et al. 2004; Lozier 2010). And recent paper introduces a data-driven eddy-resolving global ocean forecast system referred to as WenHai, possessing superior performance over state-of-the-art eddy-resolving numerical Global Ocean Forecasting Systems in simulating temperature profiles, salinity profiles, and SST fields (Cui et al. 2025). Building upon this foundation, the potential for artificial intelligence to enhance prediction capabilities for AMV and DAMV merits systematic exploration.

Apart from the OHT driven by the AMOC in a meridional dimension, we surmise that this lead-lag time may be directly linked to the sinking and upwelling processes of the NADW (Marshall and Speer 2012). Such asymmetry may further reflect additional alternative signals of asymmetry between Arctic and Antarctic warming potentially associated with climatological Antarctic Circumpolar Current and AMOC (Wang et al. 2024). However, considered that the large model biases of meridional velocity and vertical velocity in deep Atlantic, the above-mentioned surmises deserve further investigation after comprehensive estimating the simulation skills in AMV–DAMV delayed coupling based on a variety of model simulations.

This study focuses on the coupling between the SST and DSPT variations, mediated by the AMOC. However, salinity variability, particularly in the subpolar North Atlantic, also shows strong association with the AMOC, which is lacking in this study. The high salinity in the subpolar North Atlantic is a prerequisite for the AMOC, which is capable of carrying the heat and carbon from surface to deep Atlantic. Recent research points out that sea surface salinity (SSS) in the subpolar North Atlantic could be regarded as an AMOC mean state indicator on the basis of paleoclimate modeling (Dai

et al. 2025). And high coherence among the subpolar North Atlantic SST, SSS, upper ocean heat content, upper ocean salt content, and the AMOC fingerprint has been associated with the AMV in both observations and a fully coupled climate model (GFDL-CM2) (Zhang 2017). Whether a linkage or coupling exists between DAMV and SSS variability presents an interesting scientific question worthy of further investigation.

Considered the pivotal role of AMOC in the AMV–DAMV coupling, such coupling dynamics could evolve in response to changes in the strength of the AMOC. Compared with an unperturbed control simulation based on the MPI-ESM-LR, a Holocene simulation can disrupt the intrinsic AMV–AMOC connection as post-eruption periods often feature an AMOC strengthening forced by the volcanically induced surface cooling (Zanchettin et al. 2023). Given the tight connection between AMV–DAMV coupling and AMOC, investigating how the AMV–DAMV coupling evolves under volcanic forcings deserves further in-depth studied.

Finally, this study is subject to two main sources of uncertainty. (a) Consideration of observational uncertainties and structural model biases is essential for robust interpretation of the conclusions. The available deep Atlantic potential temperature data derived from observation and reanalysis are limited in both temporal and spatial coverage, resulting in inevitable uncertainties. Moreover, it is widely recognized that deep-sea variables exhibit lower inter-model consistency than sea surface variables in current model simulations (Griffies et al. 2016), underscoring the need to strengthen the robustness of DAMV through a wider range of state-of-the-art model simulations. (b) While this study is primarily data-analytical in nature, the development of a systematic theoretical framework is essential for quantitatively characterizing the DAMV as a deep-ocean symbiotic fingerprint of the AMV. Such framework would help elucidate the critical role in Atlantic climate dynamics, thereby laying the theoretical foundation for coupled decadal prediction.

Supplementary Information The online version contains supplementary material available at https://doi.org/10.1007/s00382-026-08134-y.

Acknowledgements We thank the help from Huan Guo, as helpful and detailed discussion about the GFDL-CM4 piControl simulation used in this study. Moreover, we deeply appreciate Davide Zanchettin for timely discussion and helpful sharing about the AMV sub-ensemble data from historical run in the CMIP6, which improves the robustness and reliability of conclusions effectively. In addition, we acknowledge inspired discussions about associated dynamics with Zhengguang Zhang. At last, it is grateful for the improvement about statistical results after discussions with Yazhou Zhang and Yue Sun.

Author contributions J. Y. and J. L. designed the study. J.Y. performed analysis, generated all figures and wrote the initial manuscript in discussion with Q.A. J.Y., Q.A. and J.L. contributed to finalizing the paper. L.H. contributed to offer the MOSORA reanalysis dataset of this paper and discussion of details about the dataset.

Funding This study is financially supported by National Key R&D Program of China (2023YFF0805100), Laoshan Laboratory (No. LSKJ202202600), Shandong Natural Science Foundation Project (ZR2019ZD12), and Fundamental Research Funds for the Central Universities (202242001).

Data availability Deep sea potential temperature data from the EN dataset version 4.2.2 is available online at https://www.metoffice.gov.uk/hadobs/en4/download-en4-2-2.html. And deep sea potential tem perature reanalysis from the MOSORA dataset can be addressed to the L.H. Sea Surface temperature data used in this study includes the ERSST dataset version 5 at https://psl.noaa.gov/data/gridded/data.noaa.ersst.v5.html, and the COBE version 2 at https://psl.noaa.gov/data/gridded/data.cobe2.html. The AMV index is available at https://psl.noaa.gov/data/timeseries/AMO. The CMIP6 model outputs used in this study may be downloaded freely at https://esgf-node.llnl.gov/projects/cmip6/. The ETOPO1 global relief model is at https://ngdc.noaa.gov/mgg/global/global.html. Any other data requests can be addressed to the author J.Y.

Declarations

Conflict of interest The authors declare no competing interests.

References

An QR, Li JP, Yang JJ (2024) Evaluation of sea surface temperature interhemispheric dipole in CMIP6 historical simulations. Clim Dyn 62:10347–10362

Baker JA, Bell MJ, Jackson LC et al (2025) Continued Atlantic overturning circulation even under climate extremes. Nature 638

Böning CW, Scheinert M, Dengg J et al (2006) Decadal variability of subpolar gyre transport and its reverberation in the North Atlantic overturning. Geophys Res Lett 33

Booth B, Dunstone N, Halloran P et al (2012) Aerosols implicated as a prime driver of twentieth-century North Atlantic climate variability. Nature 485:534–534

Borchert LF, Müller WA, Baehr J (2018) Atlantic Ocean heat transport influences interannual-to-decadal surface temperature predictability in the North Atlantic Region. J Clim 31:6763–6782

Bretherton CS, Smith C, Wallace JM (1992) An intercomparison of methods for finding coupled patterns in climate data. J Clim 5(6):541–560

Buckley MW, Marshall J (2016) Observations, inferences, and mechanisms of the Atlantic meridional overturning circulation: a review. Rev Geophys 54:5–63

Caesar L, Rahmstorf S, Robinson A et al (2018) Observed fingerprint of a weakening Atlantic Ocean overturning circulation. Nature 556:191–196

Casey KS, Adamec D (2002) Sea surface temperature and sea surface height variability in the North Pacific Ocean from 1993 to 1999. J Geophys Res Oceans 107

Chen XY, Tung KK (2014) Varying planetary heat sink led to global-warming slowdown and acceleration. Science 345:897–903

Cheng L, von Schuckmann K, Abraham JP et al (2022) Past and future ocean warming. Nat Rev Earth Environ 3:776–794

Cherry S (1997) Some comments on singular value decomposition analysis. J Clim 10:1759–1761

Clement A, Bellomo K, Murphy LN et al (2015) The Atlantic multidecadal oscillation without a role for ocean circulation. Science 350:320–324
Collins M, Botzet M, Carril AF et al (2006) Interannual to decadal climate predictability in the North Atlantic: a multimodel-ensemble study. J Clim 19:1195–1203
Cui YZ, Wu R, Zhang X et al (2025) Forecasting the eddying ocean with a deep neural network. Nat Commun 16
Cunningham SA, Kanzow T, Rayner D et al (2007) Temporal variability of the Atlantic meridional overturning circulation at 26.5 degrees N. Science 317:935–938
Curry RG, McCartney MS, Joyce TM (1998) Oceanic transport of subpolar climate signals to mid-depth subtropical waters. Nature 391:575–577
Dai J, Xu F, Wright JS et al (2025) Subpolar North Atlantic sea surface salinity as an AMOC mean state indicator. NPJ Clim Atmos Sci 8:308
Davis RE (1978) Predictability of sea level pressure anomalies over the North Pacific Ocean. J Phys Oceanogr 8:233–246
Delworth TL, Zeng FR (2012) Multicentennial variability of the Atlantic meridional overturning circulation and its climatic influence in a 4000 year simulation of the GFDL CM2.1 climate model. Geophys Res Lett 39
Dengler M, Schott F, Eden C et al (2004) Break-up of the Atlantic deep western boundary current into eddies at 8°S. Nature 432:1018–1020
Deser C, Alexander MA, Xie SP, Phillips AS (2010) Sea surface temperature variability: patterns and mechanisms. Ann Rev Mar Sci 2:115–143
Dickson B, Yashayaev I, Meincke J et al (2002) Rapid freshening of the deep North Atlantic Ocean over the past four decades. Nature 416:832–837
Dunne JP, Horowitz LW, Adcroft AJ et al (2020) The GFDL earth system model version 4.1 (GFDL-ESM 4.1): overall coupled model description and simulation characteristics. J Adv Model Earth Syst 12
Dunstone NJ, Smith D, Booth B et al (2013) Anthropogenic aerosol forcing of Atlantic tropical storms. Nat Geosci 6:534–539
Enfield DB, Mestas-Nuñez AM, Trimble PJ (2001) The Atlantic multidecadal oscillation and its relation to rainfall and river flows in the continental US. Geophys Res Lett 28:2077–2080
Eyring V, Bony S, Meehl GA et al (2016) Overview of the coupled model intercomparison project phase 6 (CMIP6) experimental design and organization. Geosci Model Dev 9:1937–1958
Fine RA, Rhein M, Andrié C (2002) Using a CFC effective age to estimate propagation and storage of climate anomalies in the deep western North Atlantic Ocean. Geophys Res Lett 29
Frankignoul C, Gastineau G, Kwon Y (2017) Estimation of the SST response to anthropogenic and external forcing and its impact on the Atlantic multidecadal oscillation and the Pacific decadal oscillation. J Clim 30(24):9871–9895
Gong X, Liu HL, Wang FC, Heuzé C (2022) Of Atlantic meridional overturning circulation in the CMIP6 project. Deep Sea Res Part II Top Stud Oceanogr 206
Good SA, Martin MJ, Rayner NA (2013) EN4: quality controlled ocean temperature and salinity profiles and monthly objective analyses with uncertainty estimates. J Geophys Res Oceans 118:6704–6716
Griffies SM, Danabasoglu G, Durack PJ et al (2016) OMIP contribution to CMIP6: experimental and diagnostic protocol for the physical component of the Ocean model intercomparison project. Geosci Model Dev 9:3231–3296
Gulev SK, Latif M, Keenlyside N et al (2013) North Atlantic Ocean control on surface heat flux on multidecadal timescales. Nature 499:464
Hansen J, Ruedy R, Sato M, Lo K (2010) Global surface temperature change. Rev Geophys 48
Hao X, Sein DV, Spiegl T et al (2025) Modeling the Atlantic multidecadal oscillation: the high-resolution ocean brings the timescale; the atmosphere, the amplitude. Ocean-Land-Atmos Res 4:0085
He CF, Clement AC, Kramer SM et al (2023) Tropical Atlantic multidecadal variability is dominated by external forcing. Nature 622:521
He CF, Clement AC, Cane MA et al (2022) A North Atlantic warming hole without ocean circulation. Geophys Res Lett 49
Held IM, Guo H, Adcroft A et al (2019) Structure and performance of GFDL's CM4.0 climate model. J Adv Model Earth Syst 11:3691–3727
Hermanson L, Dunstone N, Eade R, Smith D (2024) An ensemble reconstruction of ocean temperature, salinity, and the Atlantic Meridional overturning circulation 1960–2021. Q J R Meteorol Soc 150:98–111
Hirahara S, Ishii M, Fukuda Y (2014) Centennial-scale sea surface temperature analysis and its uncertainty. J Clim 27:57–75
Hirschi J, Marotzke J (2007) Reconstructing the meridional overturning circulation from boundary densities and the zonal wind stress. J Phys Oceanogr 37:743–763
Hu SN, Fedorov AV (2020) Indian Ocean warming as a driver of the North Atlantic warming hole. Nat Commun 11
Jackson LC, Biastoch A, Buckley MW et al (2022) The evolution of the North Atlantic meridional overturning circulation since 1980. Nat Rev Earth Environ 3:241–254
Kanzow T, Cunningham SA, Rayner D et al (2007) Observed flow compensation associated with the MOC at 26.5°N in the Atlantic. Science 317:938–941
Keil P, Mauritsen T, Jungclaus J et al (2020) Multiple drivers of the North Atlantic warming hole. Nat Clim Change 10:667
Kessler A, Bouttes N, Roche DM et al (2020) Atlantic meridional overturning circulation and δC variability during the last interglacial. Paleoceanogr Paleoclimatol 35
Knudsen MF, Seidenkrantz MS, Jacobsen BH, Kuijpers A (2011) Tracking the Atlantic multidecadal oscillation through the last 8,000 years. Nat Commun 2
Knudsen MF, Jacobsen BH, Seidenkrantz MS, Olsen J (2014) Evidence for external forcing of the Atlantic multidecadal oscillation since termination of the little ice age. Nat Commun 5
Kostov Y, Armour KC, Marshall J (2014) Impact of the atlanticmeridional overturning circulation on ocean heat storage and transient climate change. Geophys Res Lett 41:2108–2116
Kravtsov S, Wyatt MG, Curry JA, Tsonis AA (2014) Two contrasting views of multidecadal climate variability in the twentieth century. Geophys Res Lett 41:6881–6888
Latif M, Böning C, Willebrand J et al (2006) Is the thermohaline circulation changing? J Clim 19:4631–4637
Lau NC, Nath MJ (1994) A modeling study of the relative roles of tropical and extratropical SST anomalies in the variability of the global atmosphere ocean system. J Clim 7:1184–1207
Le Bars D, Viebahn JP, Dijkstra HA (2016) A Southern Ocean mode of multidecadal variability. Geophys Res Lett 43:2102–2110
Lee SK, Wang CZ (2010) Delayed advective oscillation of the Atlantic thermohaline circulation. J Clim 23:1254–1261
Li Y, Li JP, Feng J (2012) A teleconnection between the reduction of rainfall in Southwest Western Australia and North China. J Clim 25:8444–8461
Li Z, England MH, Groeskamp S (2023) Recent acceleration in global ocean heat accumulation by mode and intermediate waters. Nat Commun 14:6888
Lopez H, Dong SF, Lee SK, Goni G (2016) Decadal modulations of interhemispheric global atmospheric circulations and monsoons

by the South Atlantic meridional overturning circulation. J Clim 29:1831–1851
Lozier MS (2010) Deconstructing the conveyor belt. Science 328:1507–1511
Lu WY, Oppo DW, Gebbie G, Thornalley DJR (2023) Surface climate signals transmitted rapidly to deep North Atlantic throughout last millennium. Science 382:834–839
Luo FY, Ying J, Liu TY, Chen DK (2023) Origins of Southern Ocean warm sea surface temperature bias in CMIP6 models. NPJ Clim Atmos Sci 6
Mann ME, Steinman BA, Brouillette DJ, Miller SK (2021) Multidecadal climate oscillations during the past millennium driven by volcanic forcing. Science 371:1014-#x0002B;
Marshall J, Schott F (1999) Open-ocean convection: observations, theory, and models. Rev Geophys 37:1–64
Marshall J, Speer K (2012) Closure of the meridional overturning circulation through Southern Ocean upwelling. Nat Geosci 5:171–180
McCarthy GD, Brown PJ, Flagg CN et al (2020) Sustainable observations of the AMOC: methodology and technology. Rev Geophys 58:e2019RG000654
Mecking JV, Drijfhout SS (2023) The decrease in ocean heat transport in response to global warming. Nat Clim Change 13:1229-#x0002B;
Oh JH, Kug JS, An SI et al (2024) Emergent climate change patterns originating from deep ocean warming in climate mitigation scenarios. Nat Clim Change 14:260–266
Rahmstorf S, Box J, Feulner G et al (2015) Exceptional twentieth-century slowdown in Atlantic Ocean overturning circulation. Nat Clim Change 5:475–480
Rhein M, Kieke D, Steinfeldt R (2015) Advection of North Atlantic deep water from the Labrador Sea to the Southern Hemisphere. J Geophys Res Oceans 120:2471–2487
Roberts CD, Garry FK, Jackson LC (2013) A multimodel study of sea surface temperature and subsurface density fingerprints of the Atlantic meridional overturning circulation. J Clim 26:9155–9174
Schmith T, Yang ST, Gleeson E, Semmler T (2014) How much have variations in the meridional overturning circulation contributed to sea surface temperature trends since 1850? A study with the EC-Earth global climate model. J Clim 27:6343–6357
Schmitz WJ (1995) On the interbasin-scale thermohaline circulation. Rev Geophys 33:151–173
Siegelman L, Klein P, Rivière P et al (2020) Enhanced upward heat transport at deep submesoscale ocean fronts. Nat Geosci 13:50
Smethie WM, Fine RA, Putzka A, Jones EP (2000) Tracing the flow of North Atlantic Deep Water using chlorofluorocarbons. J Geophys Res Oceans 105:14297–14323
Smith DM, Allan RP, Coward AC et al (2015) Earth's energy imbalance since 1960 in observations and CMIP5 models. Geophys Res Lett 42:1205–1213
Smith DM, Murphy JM (2007) An objective ocean temperature and salinity analysis using covariances from a global climate model. J Geophys Res Oceans 112
Steinman BA, Mann ME, Miller SK (2015) Atlantic and Pacific multidecadal oscillations and Northern Hemisphere temperatures. Science 347:988–991
Sun C, Li JP, Kucharski F et al (2019) Contrasting spatial structures of Atlantic multidecadal oscillation between observations and slab ocean model simulations. Clim Dyn 52:1395–1411
Sun C, Zhang J, Li X et al (2021) Atlantic Meridional overturning circulation reconstructions and instrumentally observed multidecadal climate variability: a comparison of indicators. Int J Climatol 41:763–778
Sutton RT, McCarthy GD, Robson J et al (2018) Atlantic multidecadal variability and the UK ACSIS Program. Bull Am Meteorol Soc 99:415–425
Tamsitt V, Drake HF, Morrison AK et al (2017) Spiraling pathways of global deep waters to the surface of the Southern Ocean. Nat Commun 8
Terhaar J, Vogt L, Foukal NP (2025) Atlantic overturning inferred from air-sea heat fluxes indicates no decline since the 1960s. Nat Commun 16
Trenberth KE, Caron JM (2001) Estimates of meridional atmosphere and ocean heat transports. J Clim 14:3433–3443
Tsubouchi T, Våge K, Hansen B et al (2021) Increased ocean heat transport into the Nordic Seas and Arctic Ocean over the period 1993–2016. Nat Clim Change 11:21
Tung KK, Zhou JS (2013) Using data to attribute episodes of warming and cooling in instrumental records. Proc Natl Acad Sci U S A 110:2058–2063
Wallace JM, Smith C, Bretherton CS (1992) Singular Value Decomposition of wintertime sea-surface temperature and 500-Mb height anomalies. J Clim 5:561–576
Wang CZ, Zhang L, Lee SK et al (2014) A global perspective on CMIP5 climate model biases. Nat Clim Change 4:201–205
Wang HL, Qiu B, Liu HR, Zhang ZG (2023) Doubling of surface oceanic meridional heat transport by non-symmetry of mesoscale eddies. Nat Commun 14
Wang PX, Yang S, Li Z et al (2024) Role of the Antarctic circumpolar circulation in current asymmetric Arctic and Antarctic warming. Geophys Res Lett 51
Wills RCJ, Armour KC, Battisti DS, Hartmann DL (2019) Ocean-atmosphere dynamical coupling fundamental to the Atlantic Multidecadal Oscillation. J Clim 32:251–272
Xue JQ, Sun C, Li JP, Mao JY (2018) South Atlantic forced multidecadal teleconnection to the midlatitude South Indian Ocean. Geophys Res Lett 45:8480–8489
Yan XQ, Zhang R, Knutson TR (2018) Underestimated AMOC variability and implications for AMV and predictability in CMIP models. Geophys Res Lett 45:4319–4328
Yan XQ, Zhang R, Knutson TR (2017) The role of Atlantic overturning circulation in the recent decline of Atlantic major hurricane frequency. Nat Commun 8
Yang JJ, Li JP, An QR (2024) Deep Atlantic multidecadal variability. Geophys Res Lett 51
Yeager S, Danabasoglu G (2014) The origins of late-twentieth-century variations in the large-scale North Atlantic circulation. J Clim 27:3222–3247
Zanchettin D, Rubino A (2024) Accelerated North Atlantic surface warming reshapes the Atlantic multidecadal variability. Commun Earth Environ 5:639
Zanchettin D, Fang SW, Khodri M et al (2023) Thermohaline patterns of intrinsic Atlantic multidecadal variability in MPI-ESM-LR. Clim Dyn 61:2371–2393
Zhang R (2017) On the persistence and coherence of subpolar sea surface temperature and salinity anomalies associated with the Atlantic multidecadal variability. Geophys Res Lett 44:7865–7875
Zhang LP, Wang CZ (2013) Multidecadal North Atlantic sea surface temperature and Atlantic meridional overturning circulation variability in CMIP5 historical simulations. J Geophys Res Oceans 118:5772–5791
Zhang R, Delworth TL, Sutton R et al (2013) Have aerosols caused the observed Atlantic multidecadal variability? J Atmos Sci 70:1135–1144
Zhang R, Sutton R, Danabasoglu G et al (2019) A review of the role of the atlantic meridional overturning circulation in Atlantic multidecadal variability and associated climate impacts. Rev Geophys 57:316–375
Zhang R (2010) Latitudinal dependence of Atlantic meridional overturning circulation (AMOC) variations. Geophys Res Lett 37

Zhao J, Bower A, Yang JY, Lin XP (2018) Meridional heat transport variability induced by mesoscale processes in the subpolar North Atlantic. Nat Commun 9:1124

Zou S, Lozier MS, Buckley M (2019) How is meridional coherence maintained in the lower limb of the Atlantic meridional overturning circulation? Geophys Res Lett 46:244–252